

## FIB-Nanotomography of Particulate Systems—Part II: Particle Recognition and Effect of Boundary Truncation

Beat Münch,<sup>†</sup> Philippe Gasser, and Lorenz Holzer

Empa Materials Science and Technology, 3D-Mat, 8600 Dübendorf, Switzerland

Robert Flatt

Sika Technology AG, Corporate Research & Analytic, 8048 Zürich, Switzerland

The focused ion beam-nanotomography (FIB-nt) technique presented in Part I of this article is a novel high-resolution three-dimensional (3D) microscopy method that opens new possibilities for the microstructural investigation of fine-grained granular materials. Specifically, FIB-nt data volumes allow particle size distributions (PSD) to be determined, and the current paper discusses all the processing steps required to obtain the PSD from 3D data. This includes particle recognition and the subsequent PSD estimation. A refined watershed approach for 3D particle recognition that tolerates concavities on the particle surfaces is presented. Particles at the edge of the 3D data volume are invariably clipped, and because the data volume is of a very limited size, this effect of boundary truncation seriously affects the PSD and needs to be corrected. Therefore, two basic approaches for the stereological correction of the truncation effects are proposed and validated on artificially modeled particle data. Finally, the suggested techniques are applied to real 3D-particle data from ordinary portland cement and the resulting PSDs compared with data from laser granulometry.

### I. Introduction

QUANTITATIVE analysis in particulate systems plays an important role in the determination of fundamental structure–property relationships. This knowledge is used to optimize the corresponding materials processing steps, for example in cement and concrete technology, in ceramics, biomedicine, electronics, and optoelectronics, and in the energy/fuel cell and catalyst industries. Important attributes of granular textures are particle shape and topology of grain boundaries, particle size, and particle size distributions (PSD), number of contacts, and the geometry of particle–particle interfaces (i.e., contact curvatures).<sup>1,2</sup> Furthermore, topological aspects of long-range network structures, such as the percolation of conductive (particulate) phases, are of major interest. As many of these granular systems exhibit a high degree of disorder, quantitative determination of the relevant microstructural attributes such as those suggested by Gokhale *et al.*<sup>3</sup> can hardly be achieved based on simple 2D imaging of cross sections (e.g., scanning electron microscopy (SEM) or transmission electron microscopy (TEM)). Consequently, three-dimensional (3D) analysis is required to obtain quantitative information about granular textures.<sup>4–6</sup> The ever-increasing use of raw materials with primary particles in the submicrometer and nanometer ranges in virtually all materials science disciplines thus brings with it the necessity for high-resolution 3D microscopy methods with sub- $\mu\text{m}$  resolution.

Recently, a novel 3D microscopy method named focused ion beam-nanotomography (FIB-nt) has been developed, which enables acquisition of data volumes with a voxel resolution in the range of 20 nm, or even below<sup>7,8</sup> (for comparison: X-ray tomography usually operates with a resolution in the  $\mu\text{m}$ - or even 10- $\mu\text{m}$  range).<sup>9</sup> Part I<sup>1</sup> shows that FIB-nt has the extraordinary capability to resolve morphological details of 100 nm scale particles even from complex agglomerated and fragmented domains within the dense, grain-supported textures. However, in order to obtain such reliable particle statistics from the acquired 3D image volumes, sophisticated segmentation techniques are required to enable accurate identification of individual objects.

In conventional FIB-SEM imaging with either secondary or backscattered electrons, the contrast between the different mineral particles of a granular texture is rather low. As an alternative detection method, electron backscatter diffraction (EBSD) can also be used in FIB.<sup>10</sup> With this method, information on the crystal orientation can be obtained, which might be helpful for more detailed object recognition in dense granular textures. However, as the EBSD detection mode requires mechanical repositioning of the sample before and after each slicing/imaging cycle, this method imposes much higher acquisition times and lowers the resolution of the FIB-serial sectioning method.

As indicated by the results of our shape analysis in Part I, the statistical size–shape relationships are affected by the truncation of particles at the boundary of the acquired image volume. It appears that larger particles, and especially those with high aspect ratios, are preferentially affected by truncation at the data volume boundaries. From this example, it becomes clear that a simple statistical analysis such as PSD may be strongly biased by boundary truncation and that these effects have to be corrected.

For the extraction of reliable statistical data from 3D volumes acquired with FIB-nt, appropriate computational procedures have to be developed that are specifically valuable for the analysis of granular textures. Of particular importance are:

1. a convenient segmentation technique associated with correct particle recognition, and
2. a correction of the truncation error at the boundary of the sample volume.

In this paper, we address both topics. The segmentation problem is discussed by presenting a strategy for accurate object recognition, which is based on an enhanced watershed algorithm. Then, we focus on the truncation remedy: two different stereological procedures are presented for the correction of the boundary truncation in order to reconstruct the true PSD from the imaged volume of limited size. Furthermore, the effect of boundary truncation on the PSD and the corresponding results after stereological correction are discussed in detail. For this purpose, PSD curves are numerically simulated (with and without correction). These new algorithms are then also applied to real granular textures as obtained in Part I with FIB-nt for cement samples, and the results are compared with the corresponding data obtained by laser granulometry.

R. Riman—contributing editor

Manuscript No. 21136. Received November 9, 2005; approved April 6, 2006.

<sup>†</sup>Author to whom correspondence should be addressed. e-mail: beat.muench@empa.ch

## II. Particle Recognition

The segmentation of particle clusters from the surrounding matrix and their subsequent separation into individual grains is a widely discussed topic, and the search for the “correct fragmentation” of connected particle clusters is a rather controversial matter. There are only a few fundamental image processing tools making up the framework for various segmentation approaches<sup>11</sup>; however, for adaptation to specific tasks, these may be combined in many different ways. Small variations can dramatically impair the resulting segmentation quality. A specific problem for segmentation of dense granular materials is introduced by concave particle shapes, because similar geometries are also formed at the contact zones of touching particles. In the following section, we present a segmentation procedure specially tailored for object recognition in dense granular textures as obtained with FIB-nt. The special feature of this algorithm is a tuning facility that makes it possible to tolerate concavities up to a certain degree before a separation of neighboring objects is initiated.

### (1) Segmentation

The volume originally imaged by FIB-nt consists of a stack of sequential slices with gray value voxels forming a 3D image volume  $V(x, y, z)$  as shown in the left-hand image of Fig. 1. The subsequent segmentation process now works entirely in 3D. For segmentation of particles from FIB-nt images, the main challenge is the separation of the strongly interconnected particles.

The complete segmentation procedure is divided into three independent steps. Step one consists of unraveling all particles from the surrounding resin matrix and results in a binary mask  $M(x, y, z)$  that provides the basis for the successive particle recognition process. Step two is the identification of all particles in  $M(x, y, z)$ , whereby a cluster of interconnected particles shall be split up into a number of individual objects. Step 3 is required to determine the actual boundary limits of each particle. A detailed description of Steps 1–3 is given below.

### (2) Step 1—Defining the Particle Mask

The determination of the 3D particle mask  $M(x, y, z)$  includes automatic thresholding based on histogram characteristics. Figure 2 shows how the FIB-nt image values of typical cement particles and those of epoxy resin form two distinct peaks. Combined, the positions at the maximum ascending and descending slopes of the rather pronounced cement particle peak (Fig. 2) form appropriate threshold values  $t_l$  and  $t_u$ , respectively, for the extraction of the elementary 3D particle mask

$$M(x, y, z) = \begin{cases} 1, & \forall t_l < V(x, y, z) < t_u \\ 0, & \text{otherwise} \end{cases} \quad (1)$$

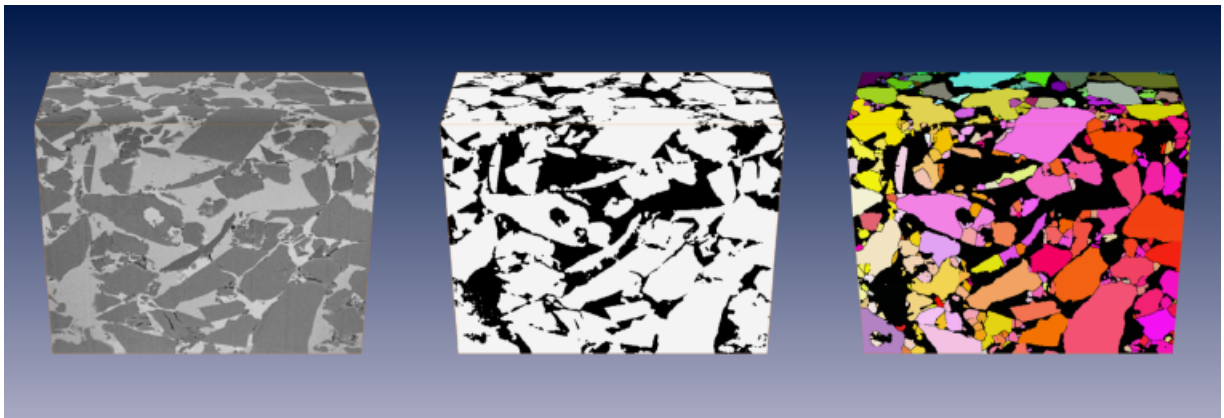


**Fig. 1.** Segmentation of a three-dimensional particle volume (scale:  $23.5 \mu\text{m} \times 19.2 \mu\text{m} \times 9.5 \mu\text{m}$ ) using the modified watershed approach. The particle mask from the original scanning electron microscopic image volume (left) is achieved by a histogram-based thresholding (center). All but a few particles are closely connected to each other. An adapted watershed segmentation algorithm is used for splitting up the particle clusters into single grains (right).

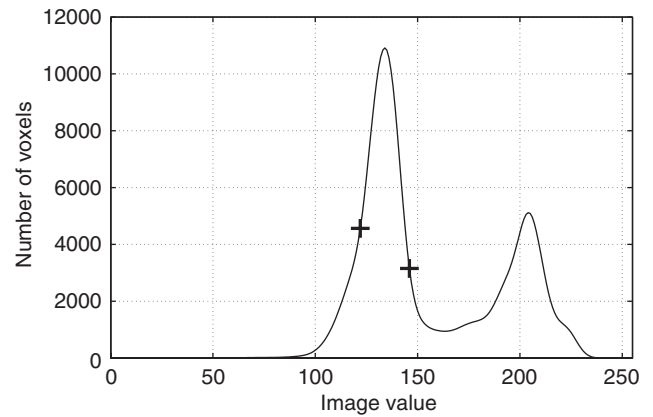


**Fig. 2.** Histogram of a particle image from focused ion beam-nanotomography. The lower and the upper thresholds,  $t_l$  and  $t_u$ , respectively, are determined by the location of the maximum and the minimum gradients in the first histogram peak formed by the particle values.

as portrayed by the middle image in Fig. 1. The FIB volume features excellent contrast between particles and matrix as well as a sufficiently high spatial homogeneity, thereby allowing the particles to be separated from the surrounding impregnation resin<sup>1</sup> by common thresholding. High voxel resolution combined with a compact point spread function guarantees that the resulting particle mask is not heavily sensitive to minor threshold shifts, allowing the threshold values to be automatically determined from the histogram characteristic (Fig. 2).

After step one, however, all particles in  $M(x, y, z)$  are still interconnected with each other (Fig. 1, center). The separation is performed by the subsequent segmentation step.

### (3) Step 2—Identification of Individual Particles

The top left picture in Fig. 3 shows a 2D section through a 3D model example of a particle mask. It consists of one single object that is composed of five overlapping particles.

A widely used approach for the fragmentation of a binary mask is the watershed segmentation algorithm.<sup>12–14</sup> It relies on the fact that eroding a binary image will cause touching features to become separated before they disappear. Conventional watershed fragmentation causes a mask  $M(x, y, z)$  to become separated at each concavity on the particle surface. As cement particles cannot be assumed to be strictly convex, the conventional watershed approach will result in much overpartitioning.

The new fragmentation concept makes use of a refined watershed technique. Here, the erosion  $j$  of the mask  $M$  is carried out by a stepwise increase in the eroding distance  $d_j$ . A particle  $p_i$  is then subdivided into  $p_{i1}, p_{i2}$  only if some fragmentation

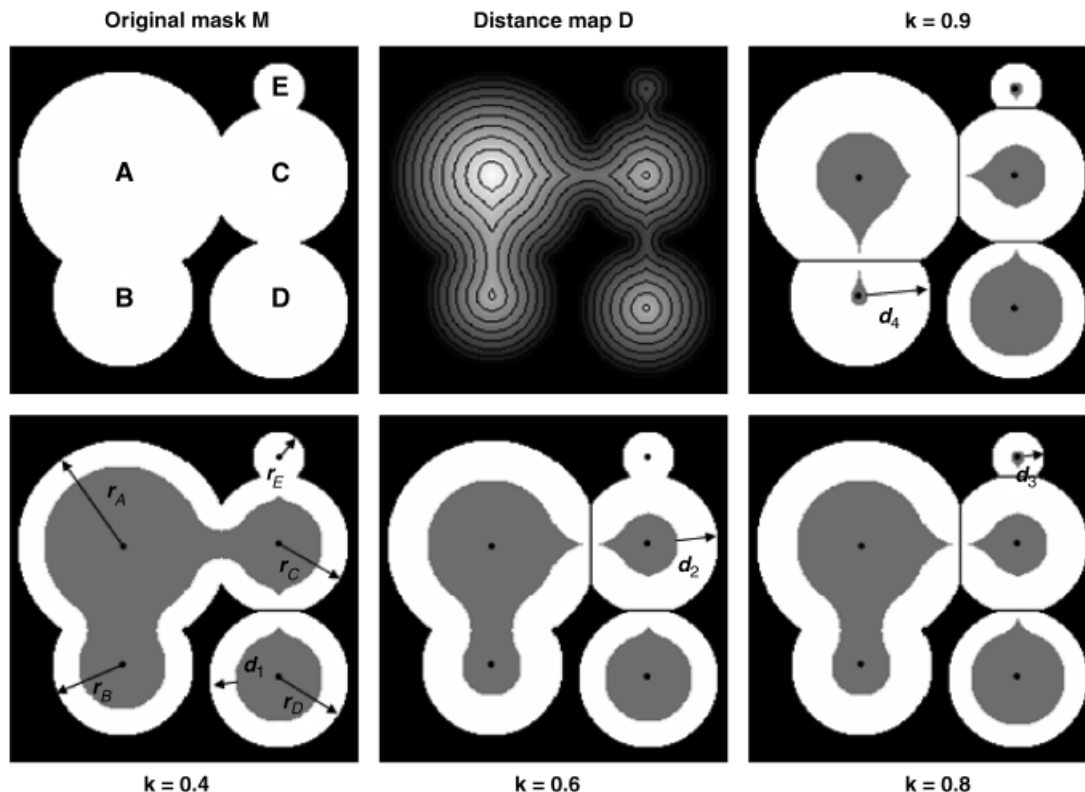


**Fig. 3.** Segmentation of a simple model with spheres. The top left image shows a particle cluster consisting of five overlapping spheres. The top center image illustrates the distance transform  $D(x, y, z)$  for fast erosion/dilation and for verifying the constraint. The top right image is the fragmentation occurring for  $k \approx 1$  or for conventional watershed segmentation. The lower row of images shows some segmentation results for varying  $k \in \{0.4, 0.6, 0.8\}$ . The gray mask illustrates the resulting labeling mask  $L(x, y, z)$  containing the positions of the fragmented particles.

constraints  $c_{i1,j}(k), c_{i2,j}(k)$  are met with

$$c_{i1,j}(k) = (d_j < kr_{p_{i1}}), c_{i2,j}(k) = (d_j < kr_{p_{i2}}) \quad (2)$$

The radii  $r_{p_{i1}}$  and  $r_{p_{i2}}$  represent the maximum distances from the interior of  $p_{i1}$  and  $p_{i2}$  to the respective surface boundaries. The constant of proportionality  $k, 0 < k < 1$  is a predefined constraint. During the fragmentation process, the eroding distance  $d_{j,j} = 1, \dots, n$  is gradually increased.

The implementation of the proposed idea makes use of the Euclidean distance transform<sup>15</sup> of the particle mask  $M(x, y, z)$ , resulting in a 3D distance map  $D(x, y, z)$  where the shortest distance to the surface is provided for any location inside of the particle mask. Based on  $D(x, y, z)$ , all erosions  $E_j$  with distance  $d_j$  are determined easily with

$$E_j(x, y, z) = \begin{cases} 1, & \forall D(x, y, z) > d_j \\ 0, & \text{otherwise} \end{cases} \quad (3)$$

After each erosion with  $d_j$ , a labeling process is implemented for all particles  $i$  in order to identify the most recent fragmentations  $F_{i,j}$  that occur when proceeding from erosion  $E_{j-1}$  to erosion  $E_j$ . Each fragmentation  $F_{i,j}$  is validated according to the constraints  $c_{i1,j}(k), c_{i2,j}(k)$  and either accepted or rejected. The predefined constant  $k$  delimits the magnitude of a constriction beyond which a fragmentation is stopped.

#### (4) Step 3—Determination of the Boundary Limits

The fragmentation just described yields a labeling mask  $L(x, y, z)$  containing the information about the positions of the cores of all the disassembled particles. Owing to the erosion processes, the particle fragments in  $L$  are reduced in size during fragmentation. With a dilation based on the distance map

$D(x, y, z)$  and the eroding distance  $d_j$ , the particles can, however, be restored to their original shape and size. This dilation process is performed by repetitively adding layers of width 1 to the eroded particles. For each layer, only those voxels at a current level of  $D(x, y, z)$  are considered. Finally, only voxels that do not cause two separated regions to become reconnected are actually added to the mask. More details about the idea and implementation of this technique are given in the literature.<sup>11,14</sup>

#### (5) Segmentation Characteristic

In conventional watershed segmentation, the regions in  $M(x, y, z)$  are totally eroded before dilating them back to the original boundaries. This implies that only entirely convex objects are not split up, as any concavity would involve a separation. Applied to regular cement particles where concavities on particle surfaces frequently occur, this leads to numerous improper fragmentations, as shown in the top right image in Fig. 4. In contrast, the proposed algorithm presented here provides a control parameter  $k$  for suitable regulation of the fragmentation, thereby allowing an appropriate segmentation to be achieved. An example of this is shown in the lower right image of Fig. 4.

The behavior of the suggested segmentation technique and the effect of  $k$  are shown in Fig. 3. The top left image displays a cross section through five spheres that overlap to various degrees. Conventional watershed segmentation results in the top right image of Fig. 3, where particles are split at any concavity. This result is correct for the current model, which intrinsically assumes five spheres. In reality, however, it is debatable whether, for instance, the sphere pair A/B actually represents two independent particles, or a single particle with surface concavities. The same question can be posed with respect to pairs C/E and A/C, and even for the cluster D/C/E. For real particles such as those displayed in Fig. 4 (top left), the result of overfragmentation by conventional watershed segmentation is dramatic (Fig. 4, top right).

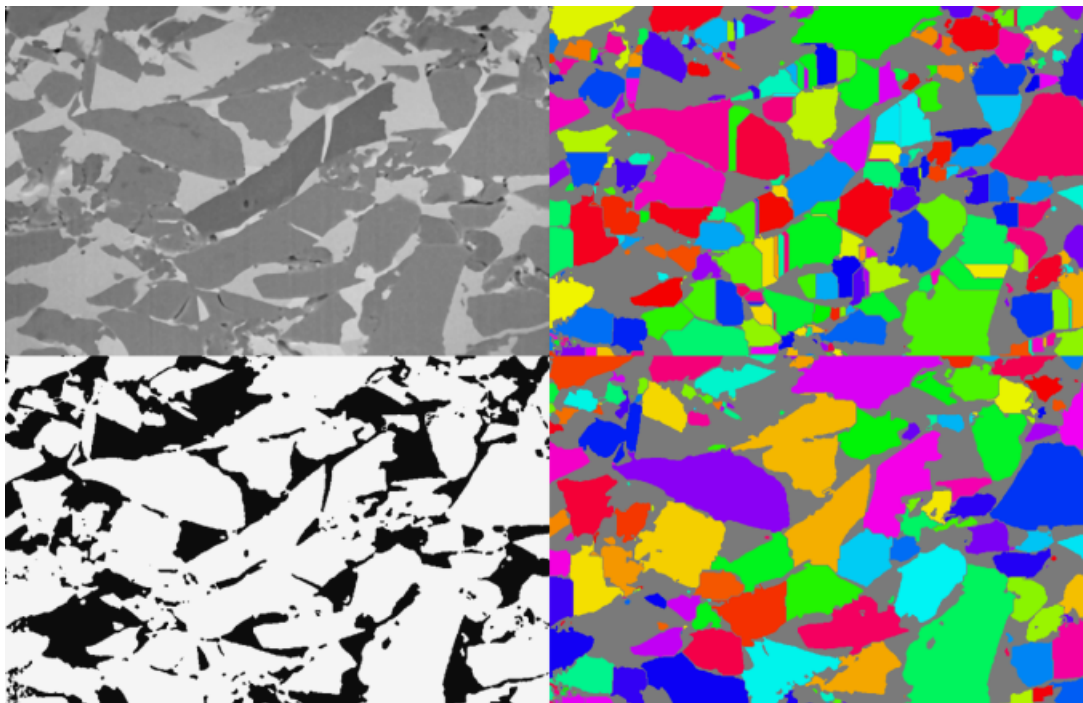


**Fig. 4.** A cross section through an original scanning electron microscopic particle volume (top left, scale:  $23.5 \mu\text{m} \times 19.2 \mu\text{m}$  at  $793 \times 509$  pixels) and its particle mask (bottom left). Due to numerous concavities, improper splitting may occur (top right). This represents the result of the unmodified watershed algorithm. The refined segmentation can be tuned with parameter  $k$  in order to produce a much more accurate fragmentation (bottom right). Notice that in order to judge the splittings, the three-dimensional progress of a particle must always be kept in mind.

In Fig. 3, the suggested algorithm yields a fragmentation into five objects for  $k > 0.8$ . For decreasing  $k$ , fragmentation reduces to concavities of increasing extent. The magnitude of concave indentation is always measured relative to the size of the particle that is under consideration to be split off. Figure 3 also shows the segmentation results for several values of the variable constraint  $k$ . Particle D exhibits a small relative overlap to its neighbor C, and is split off from the cluster already at  $k = 0.4$ . The overlap of particle pair C/E is similar in width; however, particle E is much smaller than D and is therefore not separated under  $k = 0.8$ . For  $k = 0$ , no fragmentation would occur. For the system of real particles in Fig. 4, the results for  $k = 0.9$  are displayed in the bottom right image of the figure.

The above discussion shows clearly that altering  $k$  has a significant influence on the fragmentation result when the algorithm is applied to a strongly connected mask. In the work described below, where segmentation was applied to cement particle volumes from FIB-nt, the parameter  $k$  was interactively adjusted such that the resulting segmentation would best possibly fit a visual judgment.

As also becomes obvious from Figs. 3 and 4, the decision as to how far a particle cluster is supposed to be fragmented into single particles lacks a strictly physical definition. Particularly for complex granular systems like cement powders where rapid cooling of the clinker and subsequent grinding leads to numerous internal cracks and where chemical reactivity induces agglomeration already at low relative humidity, the question of what objects should be considered as individual particles is difficult to answer. With such complex systems, FIB-nt is unique in that it permits visual inspection of a potential particle structure (Figs. 1 and 4) resulting from the application of a specific constraint  $k$  and the corresponding statistical analysis (e.g., PSD as shown in Fig. 10). This is important for the qualitative interpretation of the apparently quantitative result. Thus, in contrast to most conventional methods for particle analysis (e.g., light-scattering technique/laser diffraction, sedimentation/centrifugation, turbidity, electrosonic amplitude,<sup>17</sup>) which are based on indirect measurements including a physical model for data processing (e.g., Mie theory for light scattering<sup>18</sup>),

FIB-nt offers the possibility of a direct visual inspection and evaluation of the 3D particle structure on which the statistical results are based.

### III. Estimation of the True PSD

In addition to the analysis of higher-order topological features such as particle shape and interface geometry,<sup>1</sup> the segmentation and particle separation from FIB-nt data permits the PSD to be assessed.

For a satisfactory judgment of the proper degree of fragmentation, the best possible spatial resolution is preferable. However, as the resolution of a given FIB-nt volume increases, the number of recorded particles decreases if the data volume is kept constant. A useful compromise is thus required. For many cases, the FIB-nt data volume is relatively small and hence, the truncation of particles at the data volume boundaries introduces an additional source of error. With traditional PSD systems based on 2D imaging (e.g., particle analysis in SEM<sup>16</sup>), it is not essential to consider this error because they provide a large number of particles. Rather, the estimation of the average particle size from projected 2D particles<sup>19</sup> is the central issue there, and the truncation problem is either disregarded, or adjusted by eliminating the border particles, which is acceptable if the number of particles is very large ( $\geq 50\,000$ – $100\,000$ ). A typical FIB-nt particle volume as it is shown in Fig. 1 contains only about 2200 particles (cement fraction No. 3 in Part I of this article<sup>1</sup>), and because of this limited number of particles, the correction of the truncation effect is therefore of major importance.

A 3D PSD approach proposed by Tewari and Gokhale<sup>4</sup> bypasses the truncation problem by connecting multiple adjacent volumes and compensating the truncation bias associated with each individual volume by applying an appropriate montage technique. However, for practical reasons, multiple adjacent volumes cannot be acquired by FIB. In the case of basic particle counting, Russ<sup>20</sup> mentions two established ways to correct for the truncation problem. One way is to only consider particles touching the top and left edges of a given image and to neglect

those at the bottom and right edges. Another approach includes basic probability considerations.

In conclusion, the limitations of the inspected window size (i.e., the size of the acquired data volume) and the limited number of particles represent a considerable source of error for particle analysis with FIB-nt. The corresponding boundary problem is discussed in Section IV, where the truncation problem is analyzed and two possible remedies are proposed. In Section V, the effects of the proposed refinements are discussed in relation to modeled as well as to real particle data from FIB-nt and from laser granulometry. The latter comparison serves as a validation of the entire procedure including 3D imaging, particle recognition, and stereological correction.

#### IV. Truncation Remedy at Boundary Planes

Two alternative ways to correct for the truncation effect are proposed, namely an unspecific correction involving the total amount of particles, as well as a specific correction on the truncated particles only.

##### (1) Method A—Unspecific Correction of All Particles

The effect of particle truncation with respect to the inspected window size is first discussed in terms of probability considerations.

Suppose an inspected window  $\mathcal{W}$  of the width  $S_W$  is given together with a cubiform particle of size  $d$  and an original volume  $V_0$ , which is located at a position  $p$ , as shown in Fig. 5. The particle is visible whenever  $p$  is located within the interval  $[-d, S]$ . This interval increases as the particle size  $d$  increases and hence, the probability for larger particles to be truncated is higher than for smaller particles. This is the background why discarding border particles (see Section III) may cause an underestimation of the large volume particles relative to the small ones.

If a particle is only visible inside of  $\mathcal{W}$ , its recorded volume  $V(p)$  depends on its location  $p$ . Assuming a uniform local distribution of many such particles, the expected mean volume  $V_m$  of a particle of size  $d$  that is visible inside of  $\mathcal{W}$  is integrated to

$$V_m = \frac{1}{S+d} \int_{-d}^S V(p) dp = V_0 \frac{S}{S+d} \quad (4)$$

For  $d \ll S_W$ ,  $V_m$  approaches  $V_0$  and the correction of the truncation becomes obsolete. For 3D particle windows  $\mathcal{W}$ , featuring bounding plane sections in the  $x$ ,  $y$ , and  $z$ -directions, the volume loss due to truncation occurs for all 3D and is multiplicatively accumulated for each dimension, yielding

$$V_m = V_0 \frac{S_x S_y S_z}{(S_x + dx)(S_y + dy)(S_z + dz)} \quad (5)$$

The mean ratio  $q$  of the expected volume  $V_m$  to the original volume  $V_0$  obtained by applying Eq. (5) is displayed in Fig. 6.

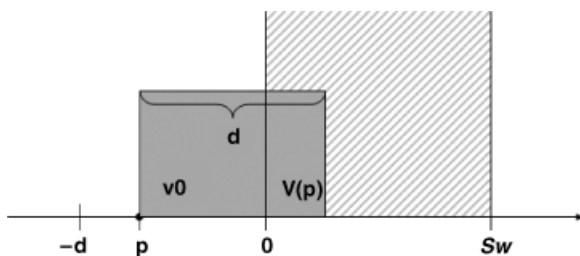


Fig. 5. A cubiform particle of dimension  $d$  which is bounded by a frame of width  $S_W$  is visible whenever  $p$  is located within  $[-d, S]$ . The size of the truncated particle strongly depends on the frame width  $S_W$ .

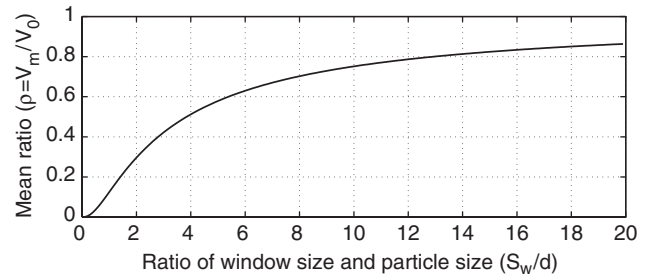


Fig. 6. Impact of the window size  $S_W$  and the particle size  $d$  on the average ratio  $r$  of the expected  $V_m$  and the true  $V_0$  three-dimensional volumes. For decreasing  $d$  relative to  $S_W$ , the average of visible volume fractions increases. For particles larger than the window size, the observed  $V_m$  becomes dramatically small.

The figure illustrates the importance of a sufficiently large imaging window  $\mathcal{W}$  relative to the largest particles in the sample. For instance, if a particle spans half of the window size, on average only 30 vol% of it will be visible inside  $\mathcal{W}$ . Less than 13 vol% of particles of the same size as the window  $\mathcal{W}$  are expected to be recorded.

Instead of taking  $q$  as a measure for the average ratio of the recorded volume for a given window  $\mathcal{W}$  and particle size  $d$ ,  $q$  may reciprocally be used as a correction factor for a particle set acquired from an image volume of a certain window size  $S_W$ . As  $q$  was calculated by considering the complete set of particles—those affected by truncation as well as those entirely included in  $\mathcal{W}$ —no differentiation is necessary when employing  $q$  as a correction factor for a PSD derived from an image volume. It should be noted here that this approach is based on the assumption of a typical particle shape, which is assumed to be a cube for Eq. (5). If the particle shapes are unknown, this might serve as a reasonable assumption.

In the remainder of this work, the correction just discussed will be referred to as an “unspecific correction,” as it is applied to the total number of particles regardless of whether they are affected by the truncation or not.

##### (2) Method B—Specific Correction of Truncated Particles Only

An alternative approach for the remedy of boundary defects that does not call for the knowledge of the particle shapes will now be introduced. It requires that the truncated particles be identified, and hence will be referred to as a “specific correction.” Fortunately, the information regarding whether or not a specific particle  $P$  is truncated by a bounding area  $A$  can be determined easily by detecting whether or not  $P$  adjoins  $A$ . Subsequently, a probability criterion for the reconstruction of the original particle size of each truncated particle is required to remedy its boundary defects.

For the determination of the expected volume  $V_m$  for a truncated particle, let  $P$  be a specific particle with an original volume  $V_0$ . Furthermore, let the particle be intersected by a plane  $A$  at position  $p$ , and the particle fraction to the left of this plane be chopped off, as shown in Fig. 7. The remaining recorded particle volume  $V(p)$  that depends on the position  $p$  of the plane  $A$  will be left over. The  $x$ -axis is defined perpendicular to the section plane  $A$ . The coordinate system is chosen relative to the particle  $P$  and the origin is chosen to lie at its barycenter.

The particle width in Fig. 7 is  $(2a)$ , i.e., it spans a horizontal range of  $[-a, a]$ . The horizontal range inside of the recorded image volume is truncated to the interval  $[p, a]$ . In 2D, a particle shape can be modeled with the help of a function  $h(x)$  describing the particle width at location  $x$ . In 3D,  $h(x)$  is defined to describe the cross-sectional area through  $P$  at location  $x$ .

Now, the volume of a particle  $P$  can be expressed by the integral of the cross-sectional area  $h(x)$  over the recorded

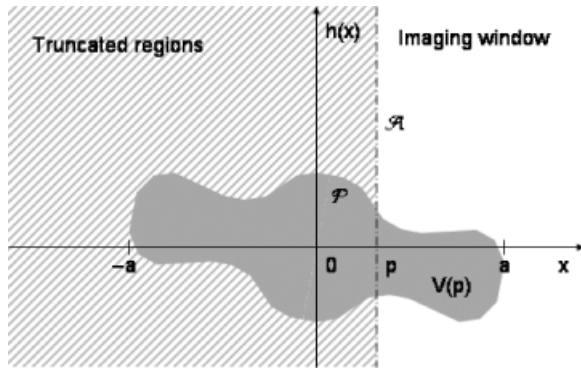


**Fig. 7.** Centrosymmetric particle which is truncated by an intersecting plane  $A$  at position  $p$ . If the abscissa is assumed to be perpendicular to  $A$  and if the actually recorded image volume is located to the right, the particle will be visible for all  $x \in [p, a]$ . The invisible truncated parts of the particle volume are shaded with a gray pattern.

range with

$$V_0 = \int_{-a}^a h(x) dx \quad (6)$$

A particle that is truncated by  $A$  at the position  $p$  retains a remaining recorded volume  $V(p)$  of

$$V(p) = \int_p^a h(x) dx \quad (7)$$

A particle is recorded by the image volume whenever the position of the boundary area  $A$  meets the condition  $p < a$ . In the case of  $p < -a$ , the particle is completely enclosed inside the image volume, and in the case  $-a < p < a$ ,  $P$  is always truncated. Thus, on average, the expected recorded volume of visible and truncated particles is given by

$$V_m = \frac{1}{2a} \int_{-a}^a V(p) dp = \frac{1}{2a} \int_{-a}^a dp \int_p^a h(x) dx \quad (8)$$

The integral in Eq. (8) can be separated into two expressions and written as

$$V_m = \frac{1}{2a} (Q - R) \text{ with } Q = \int_{-a}^a dp \int_0^a h(x) dx \quad (9)$$

$$R = \int_{-a}^a dp \int_0^p h(x) dx$$

Assuming the particle  $P$  is centrosymmetric with respect to its barycenter, thereby inducing  $h(x) = h(-x)$ , the expressions under Eq. (9) can be simplified considerably. For the term  $Q$ , this implies  $Q = Va$ . Likewise, as centrosymmetry implies that  $H(x) = -H(-x)$  where  $H(x)$  is the primitive of  $h(x)$ , the term  $R$  disappears.

In summary, Eqs. (6) through (9) yield

$$V_m = \frac{1}{2a} \int_{-a}^a dp \int_p^a h(x) dx = \frac{1}{2} \int_{-a}^a h(x) dx = \frac{1}{2} V_0 \quad (10)$$

When omitting the assumption of centrosymmetric shapes, the above considerations still remain valid provided that the particles are assumed to be randomly oriented. In order to show this, let a set of particles  $P_i, i \in \{1, \dots, m\}$  of uniform cross-sectional area  $h(x)$  be examined. Considering an arbitrary angular alignment of  $P_i$ , the average over a large number of particles (i.e., large  $m$ ) becomes rotationally symmetric. As rotational symmetry is a special case of centrosymmetry, the above con-

siderations apply for particles of *any* shape  $h(x)$  under the assumption of random orientation.

Equation (10) proves that if a particle is truncated by one single plane, its original size is expected to be twice as large on average. The only precondition is a random orientation of the particles. In 3D volumes, a particle  $P$  might be truncated by one, two, or three bounding planes at the same time, depending on whether  $P$  adjoins a single face, an edge, or a vertex. For each additional intersecting plane, the above findings are cumulated. Thus, if a particle is intersected by  $n$  adjacent planes, its original volume  $V_0$  is expected to correspond to the experimentally acquired truncated volume  $V$  enlarged by a factor  $\xi$ .

$$V_0 = \xi V, \xi = 2^n \quad (11)$$

The correction according to Eq. (11) (Method B) is specifically applied to each single particle that is affected by truncation. This is in contrast to Method A where the values of the total PSD are corrected.

## V. Discussion of the Particle Truncation Corrections

The following section contains a further discussion about the impact of particle truncation by performing numerical simulation and analysis of true FIB-nt data, and about the effect of the correction methods proposed in Sections IV (1) and (2) for remedying truncation errors.

### (1) Numerical Modeling

A set of  $n = 1\,000\,000$  uniformly distributed and randomly sized cuboid-shaped particles was modeled. Each particle was individually inserted into a new frame  $\mathcal{W}$  with dimensions  $S_{\mathcal{W}}$  at a random location. For each new particle added, the resulting particle size after truncation by  $\mathcal{W}$  was successively added to the PSD statistics. As each particle was entered into an empty window, no interparticle overlap was considered, thus validating the effect of truncation only. The side length of the cubes was chosen to follow a Gaussian distribution with a mean value of  $\mu = 700$  [units] and a standard deviation of  $\sigma = 4/7$ . Possible negative values were reflected to the zero line. The corresponding particle diameter sphere equivalent  $d_i = \sqrt[3]{\frac{6V_i}{\pi}}$  was taken as the basis for the histogram classes. The large number of particles used for numerical validation represents a sound statistical basis. For comparison, the SEM particle analysis in Part I of this article was achieved with  $n = 50\,000$  particles.

Figure 8, top left, shows the uncorrected histogram of the particles with reference to the particle diameter  $d$  as a function of varying window size. The displayed data set must be understood as the mean distribution that results from a large number of independent particle acquisition steps. The diameter range is split into equally sized bins with widths of 50[units], hence the stair-like characteristic of the curves. The black curve represents the unconstrained original particle distribution. If the particle set is narrowed by a decreasing inspection window  $\mathcal{W}$  of size  $S_{\mathcal{W}}$ , the resulting particle size apparently moves toward lower  $d$ . In cases where the particle spans the entire window  $\mathcal{W}$  in a given dimension, it is truncated to the respective window width. This is the reason why for  $S_{\mathcal{W}} = 500$ [units] (red curve), the largest particles attain a diameter of 620.35[units]. Consequently, the last bin of the histogram at the 600–700[units] interval contains a comparatively large number of particles by holding all of the largest particles.

The top right graph in Fig. 8 shows the results of a simple correction where the truncated particles are entirely omitted. If  $S_{\mathcal{W}}$  is small relative to  $d_i$  (i.e., smaller than about twice the mean particle size), the resulting PSD histograms become strongly distorted. It has to be emphasized that in real examinations, the particle count will be dramatically reduced for small  $S_{\mathcal{W}}/d_i$  by omitting truncated particles. In contrast, the particle count  $n = 1\,000\,000$  remained fixed for the modeling performed here.

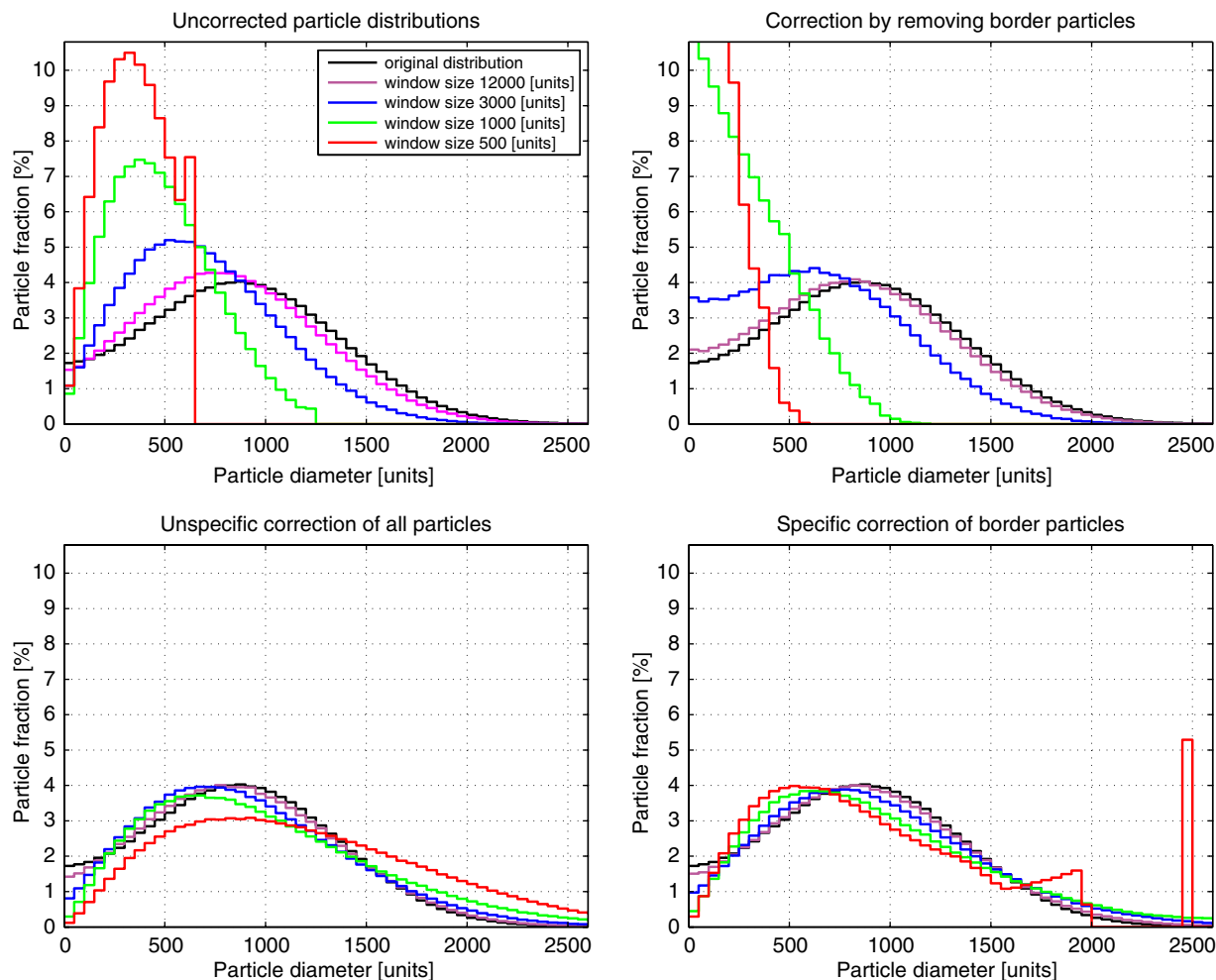


**Fig. 8.** Impact of the inspected window size on the resulting particle distribution. A set of cuboid particles with originally Gaussian-distributed side lengths ( $\mu = 700$ [units],  $\sigma = 4/7$ ) is limited by a vision panel of a variable size. The particle distributions resulting from the different window sizes are displayed together with the original distribution (top left graph). Particle analysis software (e.g., for automated scanning electron microscopic analysis) usually enables omission of particles located at the edge of the examined window. This approach causes the number of large particles to be increasingly underestimated as the size of the inspected window  $\mathcal{W}$  decreases (top right graph). After correction according to Method A, the agreement with the original unbounded distribution is considerably improved (bottom left graph), except for the smallest window where the average particle size is larger than the inspected window size  $S_{\mathcal{W}}$ . The correction according to Method B again yields a good agreement with the original particle size distributions, except for an average particle size larger than  $S_{\mathcal{W}}$  (bottom right graph).

The bottom left graph in Fig. 8 shows the same data as presented at the top left, but after correction according to unspecific Method A. The deviation from the true distribution (black curve) is small, unless the inspected window size falls below the mean particle dimensions ( $\bar{d} > S_{\mathcal{W}}$ ).

As the particle shape was taken to be a cuboid for the simulations and the correction by Method A also presupposes this particle geometry, the good agreement after correction is not unexpected. However, if the particle shape strongly differs from a cuboid, the accuracy of the correction may suffer considerably, as will be observed for the example of real cement particles (Figs. 10 and 12).

Correction with specific Method B is independent of the particle shape, but it requires knowledge of the number of planes  $n$  each particle is truncated by. The bottom right graph in Fig. 8 shows the results after correction according to Method B (Eq. (11)). The results also show a good match with the original particle size distribution, provided that  $S_{\mathcal{W}}$  is sufficiently large. For  $\bar{d} > S_{\mathcal{W}}$ , the expected particle size actually becomes unpredictable, as such particles may span the entire window width and accordingly the assumptions for Eq. (11) are only valid as an approximation.

So far, only the particle size histograms have been discussed; however, reference to volume fractions (i.e., the so-called cumulative size distribution curves) is more customary in particle

analysis. The effect of the above simulations on the resulting volume fractions is shown in Fig. 9. The results arise from the same model assumptions at the same  $S_{\mathcal{W}}$  as in Fig. 8.

The measured results and the true volume fractions again become increasingly separated from each other with decreasing  $S_{\mathcal{W}}$ . Elimination of the truncated particles proves not to be applicable for this case of polydisperse PSDs. In contrast, both corrections A and B give good approximations to the true volume fractions at  $d_{\mathcal{W}}$ . However, for the smallest window size  $S_{\mathcal{W}} = 500$ [units] where many particles are larger than  $S_{\mathcal{W}}$ , the results from Method B are considerably better than the results corrected by Method A. This is also indicated by the comparison of mean square errors  $\bar{\epsilon}_m$  for the PSD data, which are listed in Table I. As an additional measure, the relative errors of the volume fractions at 97%, 50%, and 3% ( $d_{97}$ ,  $d_{50}$ ,  $d_{03}$ ) are listed for the different correction methods. Method B yields the smallest mean square errors for all window sizes, but the advantage over the other methods is particularly large for the smallest window size. Here, an overall reduction by a factor of 8.4 is achieved for Method B compared with Method A. In view of the progression of  $d_{50}$  at descending  $S_{\mathcal{W}}$ , it can be stated that the proposed corrections are valid up to a ratio of mean particle size  $\bar{d}$  to window size  $S_{\mathcal{W}}$  of not more than  $\frac{\bar{d}}{S_{\mathcal{W}}} < 1$ . This range of tolerance is not too large to make FIB data acquisition too time intensive, so that FIB can well be used to determine PSD.

**Table I. Mean Square Errors  $\bar{\epsilon}_m$ , and Relative Errors of the Fractions  $d_{97}$ ,  $d_{50}$ ,  $d_{03}$  in [%] of the Recorded PSD Data, as a Function of the Correction Method**

$S_W$	Measured particles				Without truncated particles				Correction Method A				Correction Method B			
	$\bar{\epsilon}_m$	$\epsilon(d_{97})$	$\epsilon(d_{50})$	$\epsilon(d_{03})$	$\bar{\epsilon}_m(d_{97})$	$\epsilon(d_{97})$	$\epsilon(d_{50})$	$\epsilon(d_{03})$	$\bar{\epsilon}_m$	$\epsilon(d_{97})$	$\epsilon(d_{50})$	$\epsilon(d_{03})$	$\bar{\epsilon}_m$	$\epsilon(d_{97})$	$\epsilon(d_{50})$	$\epsilon(d_{03})$
500	795.4	74.7	68.3	71.9	795.4	80.0	80.1	85.9	175.7	42.0	35.0	57.3	21.0	0.7	11.4	40.0
1000	283.8	50.2	49.4	57.1	283.8	58.5	59.1	67.9	12.9	10.4	8.1	41.0	12.1	57.6	3.0	26.2
3000	44.3	17.3	22.8	31.2	44.3	16.7	20.0	27.8	9.4	36.3	7.4	18.8	2.6	21.8	0.8	13.7
12000	3.3	4.5	6.7	10.2	3.3	3.7	4.9	7.4	1.9	12.8	3.9	5.3	0.2	5.8	0.9	4.3

PSD, particle size distributions.

So far, particles with a Gaussian distribution of sizes have been used for assessing the correction methods A and B. Figure 11 shows the case where a collection of monosized particles is simulated. A set of  $n = 1\,000\,000$  monosized cubes with side length  $\mu = 500$ [units] is considered for a window width  $S_W = 1000$ [units]. While a perfect agreement is achieved between the real PSD (black) and the one recorded after omitting all truncated particles (magenta), the originally measured PSD as well as corrections A and B deviate from the real PSD. The example shows that omitting truncated particles from the statistics of measured values yields the best results for monosized samples. This also holds true for very narrow size distributions as the particles entirely inside of  $\mathcal{W}$  exactly represent the standard particles.

**(2) Correcting the Truncation Effect for Cement Powder Particles**

The previous analyses have focused on simulated particles. Although cuboid-shaped model particles were chosen that exactly meet the assumptions for Method A, the more general Method B provides a correction that exhibits an even higher accuracy than Method A for this predefined particle shape. As Figs. 1 and 4 show, real particle distributions as observed in cement powder do not offer the benefit of known particle shapes and this causes additional uncertainty when Method A is applied.

In Part I of this contribution,<sup>1</sup> several grain size fractions of cement powder were measured using FIB-nt. Of these, fraction No. 3 is used in this paper to evaluate the data processing steps, and it is this material whose FIB-nt data are shown in its raw

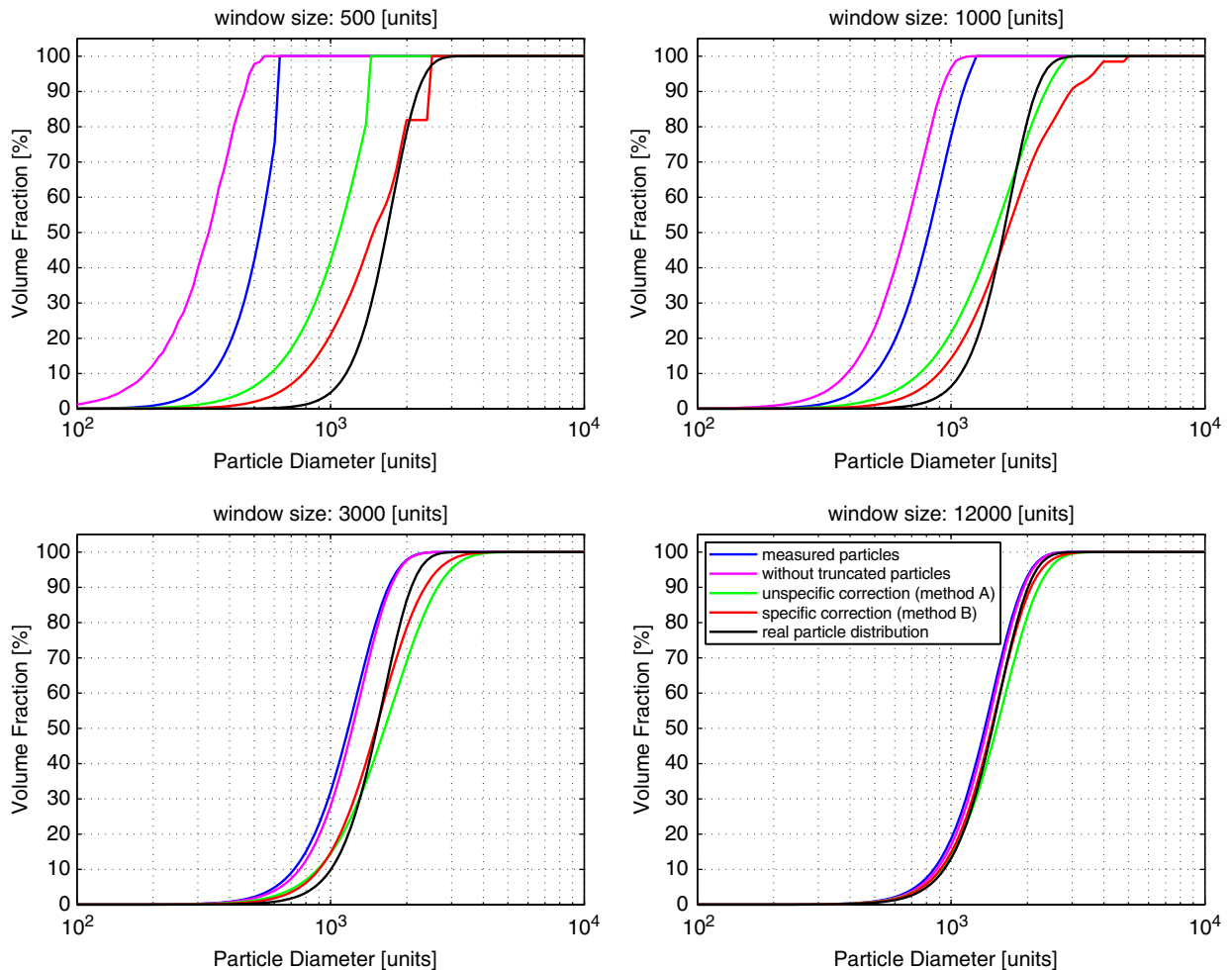


**Fig. 9.** Resulting volume fractions after limitation of the examined window size. A set of 1 000 000 cuboid particles with originally Gaussian-distributed side lengths with a mean of  $\mu = 700$ [units] and a standard deviation of  $\sigma = 4/7$  was analyzed using four different window sizes of 500, 1000, 3000, 12 000[units] (same settings as in Fig. 8). A plot is provided for each window size, with each plot showing the original progression of the volume fraction in black, together with the one gathered by evaluating the originally acquired particle set (blue), the particle set without the truncated particles (magenta), as well as the particle set corrected according to Method A (green) and Method B (red).

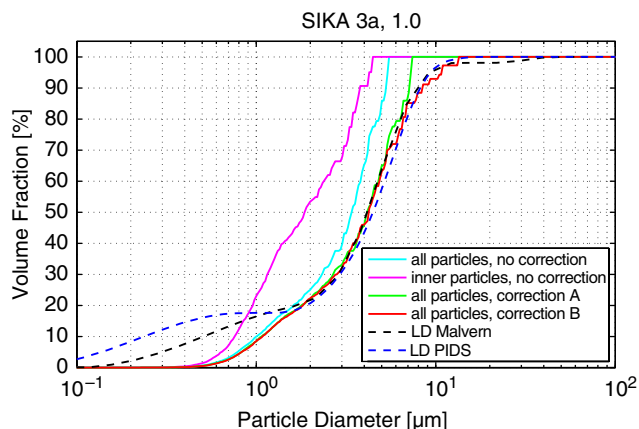


**Fig. 10.** Volume fractions from cement particles of grain size fraction No. 3 as measured in Part I of this contribution.<sup>1</sup> The ratio of the inspected frame size relative to the particle diameter at  $d_{50}$  is about 3:1. In addition to the original particle size distribution (PSD) obtained with focused ion beam and its corrected versions, the PSD from two common laser diffraction methods are also shown.

and segmented states in Figs. 1 and 4. The corresponding PSD results after particle fragmentation and stereological correction are shown in Fig. 10. The constant  $k = 0.9$  was chosen such that the resulting particle fragmentation would well meet a visual overall judgment of the entire volume. The particles at  $d_{50}$  exhibit a typical diameter of about  $1/3$  of the smallest window dimension  $S_{Wz}$ . This situation is comparable to the simulated particle sets at  $S_W = 3000$ [units] (bottom left graph in Fig. 9).

While the true PSD characteristics are available only for the simulations, they are not precisely known for cement powder fractions. Instead, it is useful to compare the PSD characteristic from FIB-nt with distributions acquired using other widely used particle sizing techniques. For this purpose, the PSD of cement fraction No. 3 was measured using laser diffraction (LD), and laser diffraction with polarization intensity differential scattering (PIDS). In the remainder of the text, these two methods are referred to as LD-Malvern (referring to the instrument built by Malvern Instruments Ltd., Malvern, UK, which was used) and LD-PIDS, respectively.

While for particles larger than  $\sim 1.0 \mu\text{m}$  there is a close agreement of both LD measurements with the FIB-nt PSD analysis corrected with either Methods A or B, a certain mismatch occurs for smaller particles (Fig. 10). Indeed, LD is not suitable for classifying particles of a size below the wavelength of the applied laser (LD-Malvern:  $\lambda = 633 \text{ nm}$ , LD-PIDS:  $\lambda = 450/600/900 \text{ nm}$ ).

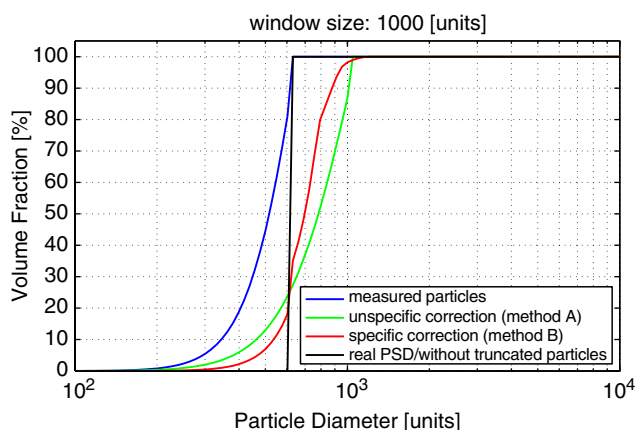


**Fig. 11.** Particle size distribution (PSD) of 1 000 000 equisized cuboid particles and its broadening due to the inspection window with  $S_W = 1000$ [units]. The black curve illustrates the true PSD, which exactly matches the recorded PSD from which the truncated particles have been omitted.

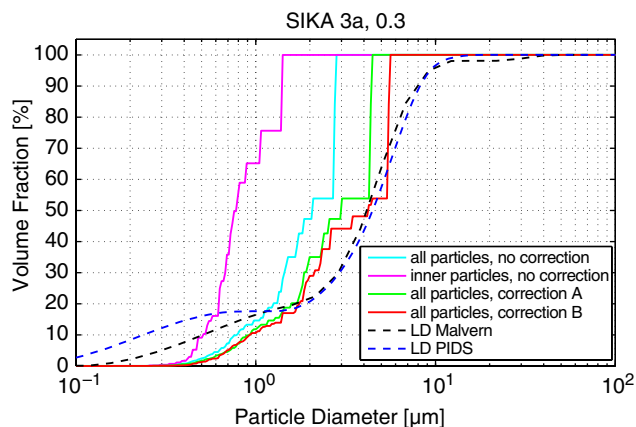


**Fig. 12.** Particle size distribution (PSD) measurements of the same grain size fraction No. 3 as in Fig. 10, but after clipping the inspected focused ion beam-nanotomography volume by a factor of 0.3 in all three dimension ( $x, y, z$ ). The PSD measurements obtained by Malvern and polarization intensity differential scattering laser diffraction (Fig. 10) are provided for comparison.

Under such conditions, sharp edges on particle surfaces will be interpreted as particles of that scale. In contrast, the mean voxel resolution for the acquired FIB-nt data from fraction No. 3 is 42 nm. This resolution is sufficient for the analysis of particles in the range between 400 nm and  $1 \mu\text{m}$ , and therefore FIB-nt is a significantly more reliable technique than LD for the sizing of submicron particles. The very good match for particles larger than  $1 \mu\text{m}$  where LD methods are reliable confirms that the total procedure including FIB-nt imaging, particle recognition, and stereological correction by both methods (A and B) can be validated by laser granulometry. The comparison of PSDs obtained with FIB-nt versus other techniques will be the subject of a following paper.

The quality of the corrected distributions in Fig. 10 was examined further by investigating whether or not they remain stationary when the inspected window size  $S_W$  is reduced. The original window size used for the analysis of grain size fraction No. 3 is given by  $S_W = 23.5 \mu\text{m} \times 19.2 \mu\text{m} \times 9.5 \mu\text{m}$ .<sup>1</sup> From this original sample, a subvolume with the  $x, y, z$  dimensions reduced by a factor of 0.3 each was extracted, leaving a total volume of only  $1/37$  of the raw volume ( $S_W = 7.05 \times 5.67 \times 2.85 \mu\text{m}^3$ ). This volume reduction is roughly equivalent to the reduction of  $S_W = 3000$ [units] down to  $S_W = 1000$ [units] (Section V (I), Fig. 9).

The results are shown in Fig. 12, again in relation to the LD measurements discussed above. The measured fraction changes significantly for large particles (mean square error  $\varepsilon(d_{50}) = 39.4\%$  and the accuracy deteriorates even further when omitting the truncated particles due to an underestimation of the large particles ( $\varepsilon(d_{50}) = 58.2\%$ ). In contrast, the volume fractions corrected according to Methods A and B remain more stable with the reduction in the analyzed volume (Method A:  $\varepsilon(d_{50}) = 28.2\%$ , Method B:  $\varepsilon(d_{50}) = 0.4\%$ ). Here, the greatest deviations occur for the largest particles. The observed step-like shape of the PSD curves is attributed to the small particle count. Especially for large particles, these steps considerably increase in width after a correction is applied because large particles are subject to particularly strong corrections.

## VI. Conclusions

Thus, it has been demonstrated that the novel FIB-nt technique is not only an excellent approach for the acquisition of real 3D data for microstructural analysis but is also a powerful tool for generating particle size distributions. The method possesses a spatial resolution that is sufficient to characterize even the smallest size fractions of finely divided particulate materials, as demonstrated on the example of cement powder in this work.

The computational techniques for object recognition and for correction of truncation effects presented in this paper are the basis for reliable statistical characterization of granular textures. The particular power of the method is that for the first time it is possible to compare a PSD characteristic relative to the particle fragmentation with which it is associated. This is especially useful for the analysis of cement fractions because particles in these materials form agglomerates of quasi-fractal appearance where identification of the grain boundaries becomes ambiguous. The enhanced watershed segmentation method introduced here is able to cope with this microstructural complexity because the specific amount of fragmentation can be controlled with the adjustable parameter  $k$ . Thus, a major advantage of the FIB-nt PSD technique is that the fragmentation result can be visually evaluated in true 3D and regenerated with an adjusted value of  $k$  if the result is not physically tenable.

A problematical issue with the technique is that the acquisition of FIB-nt volumes is a time-consuming process, and therefore it is desirable to keep the acquired volumes as small as possible. With such small data sets, however, the original image data are strongly affected by the truncation of the particles at the sample boundaries. Two appropriate remedies have been proposed and verified on model calculations and on practical 3D measurements of real cement particles. Comparison with data from two conventional PSD methods showed that after these corrections are applied, the FIB-nt PSD results give reliable estimates of the effective size distribution.

In future, FIB-nt may also be applied to the analysis of granular textures in solid bodies of material. The ability to use the technique on densified bulk material is a distinct advantage over conventional methods such as laser diffraction, which are only applicable to suspensions and loose powders. FIB-nt, in combination with the presented computational techniques, thus lay the foundations for quantitative microstructural analysis of fine-structured granular materials such as particle-reinforced ceramic-composite materials<sup>5</sup> and cryo-stabilized suspensions of cement pastes.<sup>21</sup>

## References

<sup>1</sup>L. Holzer, B. Münch, M. Wegmann, R. J. Flatt, and Ph. Gasser, "FIB-nanotomography of particulate systems—Part I: Particle shape and topology of interfaces." *J. Am. Ceram. Soc.*, **89** [8] 2577–2585(2006).

<sup>2</sup>L. B. Wang, J. D. Frost, and J. S. Lai, "Three-Dimensional Digital Representation of Granular Material Microstructure from X-Ray Tomography Imaging." *J. Comput. Civil Eng.*, **18** [1] 28–35 (2004).

<sup>3</sup>A. Gokhale, W. J. Drury, and B. Whited, "Quantitative Microstructural Analysis of Anisotropic Materials," *Mater. Charact.*, **31** [1] 11–7 (1993).

<sup>4</sup>A. Tewari and A. M. Gokhale, "Estimation of Three-Dimensional Grain Size Distribution From Microstructural Serial Sections," *Mater. Charact.*, **46**, 329–35 (2001).

<sup>5</sup>N. Chawla, V. V. Ganesh, and B. Wunsch, "Three-dimensional (3D) Microstructure Visualization and Finite Element Modeling of the Mechanical Behavior of SiC Particle Reinforced Aluminum Composites," *Scripta Mater.*, **51** [2] 161–5 (2004).

<sup>6</sup>H. Singh and A. M. Gokhale, "Visualization of Three-Dimensional Microstructures," *Mater. Charact.*, **54**, 2475–87 (2004).

<sup>7</sup>L. Holzer, F. Indutnyi, P. Gasser, B. Münch, and M. Wegmann, "Three-Dimensional Analysis of Porous BaTiO<sub>3</sub> Ceramics Using FIB Nanotomography," *J. Microsc.*, **216** [1] 84–95 (2004).

<sup>8</sup>A. J. Kubis, G. J. Shiflet, D. N. Dunn, and R. Hull, "Focused Ion-Beam Tomography," *Metall. Mater. Trans. A*, **35A**, 1935–43 (2004).

<sup>9</sup>L. Babout, E. Maire, and R. Fougères, "Damage Initiation in Model Metallic Materials: X-ray Tomography and Modeling," *Acta Mater.*, **52**, 21–9 (2005).

<sup>10</sup>M. D. Uchic, M. Groeber, and R. Wheeler, "Augmenting the 3D Characterization Capability of the Dual Beam FIB-SEM," *Microsc. Microanal.*, **10** [2] 1136–7 (2004).

<sup>11</sup>J. C. Russ, *The Image Processing Handbook*, 3rd edition, pp. 371–429, 494–8. CRC Press, Boca Raton, FL, 1999.

<sup>12</sup>S. Beucher and C. Lantuéjoul, "Use of Watersheds in Contour Detection"; pp. 17–21 in *Proceedings of the International Workshop Image Processing, Real-Time Edge and Motion Detection/Estimation, Rennes, France, September 17–21, 1979*.

<sup>13</sup>C. Lantuéjoul and S. Beucher, "On the Use of the Geodesic Metric in Image Analysis," *J. Microsc.*, **121** [1] 29–49 (1980).

<sup>14</sup>J. C. Russ and J. C. Russ, "Improved Implementation of a Convex Segmentation Algorithm," *Acta Stereol.*, **7** [1] 33–40 (1988).

<sup>15</sup>J. H. Friedman, J. L. Bentley, and R. A. Finkel, "An Algorithm for Finding Best Matches in Logarithmic Expected Time," *ACM Trans. Math. Software*, **3** [3] 209–26 (1977).

<sup>16</sup>M. Y. Abyaneh, M. J. Keedwell, and C. Leppard, "Scanning Electron Micrographs and Their Interpretation in the Context of a Theory Proposed for the Hardening Behaviour of Cementitious Materials," *Adv. Cement Res.*, **13** [3] 131–7 (2001).

<sup>17</sup>D. M. Scott, "Characterizing Particle Characterization," *Particle Particle Systems Charact.*, **20**, 305–10 (2003).

<sup>18</sup>G. Mie, "Beiträge zur Optik trüber Medien, speziell kolloidaler Metallösungen," *Ann. Phys.*, **25** [4] 377–455 (1908).

<sup>19</sup>A. M. Gokhale and V. Benes, "Estimation of Average Particle Size from Vertical Projections," *J. Microsc.*, **191** [2] 195–200 (1998).

<sup>20</sup>J. C. Russ, *The Image Processing Handbook*, 3rd edition, pp. 529–32 CRC Press, Boca Raton, FL, 1999.

<sup>21</sup>L. Holzer, B. Münch, and P. Gasser, "New approaches in microstructure analysis of cementitious materials: From micro to nano, from 2D to 3D and from qualitative to quantitative characterization"; *Second International Symposium on Nanotechnology in Construction (NICOM2)*, RILEM, Bilbao (S), 2005, in press □